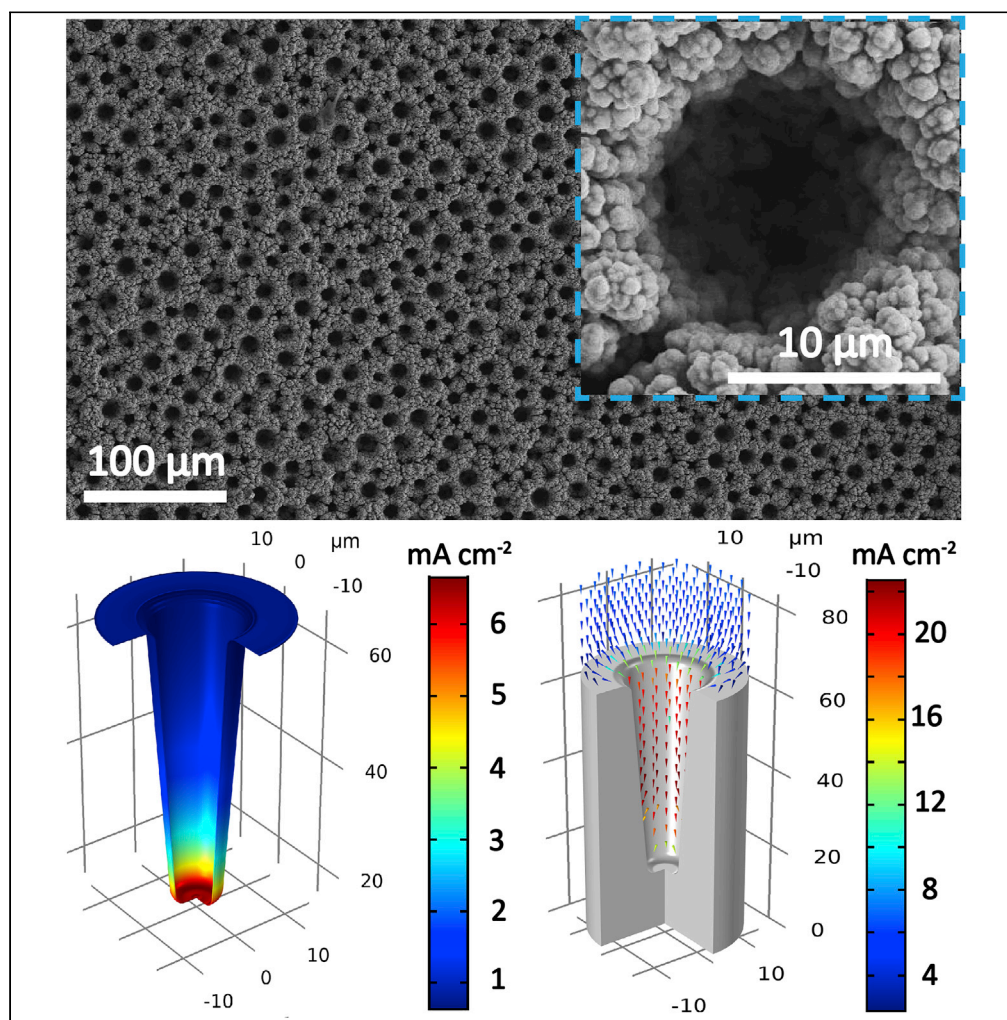## Article

Uniform Li Plating/Stripping within Ni Macropore Arrays Enabled by Regulated Electric Field Distribution for Ultra-Stable Li-Metal Anodes

Yang Yang, Jinfei Xiao, Chaoyue Liu, ..., Jinbao Zhao, Cheng Chao Li, Weidong He

licc@gdut.edu.cn (C.C.L.)
weidong.he@hit.edu.cn (W.H.)

HIGHLIGHTS

The Ni macropore arrays electrode is fabricated by a facile electrodeposition method

The regulated electric field distribution leads to stable Li deposition behavior

The LiFePO$_4$ || Li-Ni macropore arrays full cell shows excellent cycling stability

Article

Uniform Li Plating/Stripping within Ni Macropore Arrays Enabled by Regulated Electric Field Distribution for Ultra-Stable Li-Metal Anodes

Yang Yang,[1] Jinfei Xiao,[1] Chaoyue Liu,[2] Dongjiang Chen,[3] Hongbo Geng,[1] Yufei Zhang,[1] Jinbao Zhao,[2] Cheng Chao Li,[1,4,*] and Weidong He[3,*]

SUMMARY

Although Li-metal anodes are extremely attractive owing to the ultrahigh theoretical specific capacity, the low Coulombic efficiency and severe safety hazards resulting from uncontrollable Li dendrites growth hinder their widespread implementation. Herein, we propose a novel design of Ni macropore arrays for the functional Li deposition host. Benefiting from the regulated electric field distribution, Li nucleation and growth can be well confined within conductive Ni macropores. Consequently, the Ni macropore array electrode exhibits stable Li deposition behavior, i.e., high Coulombic efficiency of above 97% over 400 cycles for 1.0 mAh cm^{-2}. Most importantly, the LiFePO$_4$ ‖ Li-Ni macropore arrays full cell also shows greatly enhanced cycling stability (90.3 mAh g^{-1} at 1 C after 700 cycles), holding great promise for high-performance rechargeable Li metal batteries.

INTRODUCTION

The 2019 Nobel Prize in chemistry has been jointly given to John. B. Goodenough, M. Stanley Whittingham, and Akira Yoshino, awarding their pioneering work to production of lithium-ion batteries (LIBs). With the continuous advancement of battery technology, LIBs have dominated the market of portable electronic devices and electric vehicles. However, the limited theoretical capacity of state-of-the-art graphite anode (372 mAh g^{-1}) severely impedes the ever-increasing demand for higher energy density of LIBs (McDowell et al., 2013; Tarascon and Armand, 2001). Li metal, the well-accepted "holy grail" electrode, has received widespread concern owing to its high gravimetric specific capacity (3,860 mAh g^{-1}) and the lowest redox potential (−3.040 V versus standard hydrogen electrode [SHE]) (Liang et al., 2016; Winter et al., 2018). Meanwhile, Li metal anode is also an indispensable component for new-generation batteries such as lithium-air and lithium-sulfur batteries.

Even though Li metal batteries were once attempted to be commercialized by Moli Energy early in the 1980s, serious safety issues and short lifespan resulted in their withdrawal from the market (Li et al., 2018). The two main bottlenecks of Li metal anodes are the formation of Li dendrites and infinite volume change during cycling. More specifically, the uncontrollable growth of Li dendrites may penetrate the separator, leading to the internal short circuit and battery failure. Besides, Li plating is a "host-less" electrodeposition process with the infinite volume change, which will lead to the crack of solid electrolyte interface (SEI) film. And the repeated cracking and repair of SEI would persistently consume the electrolyte and form isolated "dead Li," resulting in unsatisfactory Coulombic efficiency (CE) and short cycle life.

To date, numerous approaches have been developed to improve the electrochemical performance of Li-metal anodes. One feasible method to restrain dendrite growth focuses on the modification of electrode/electrolyte interphase, such as adding appropriate additives to the electrolyte to stabilize SEI (Wu et al., 2017; Yang et al., 2019a; Zhang et al., 2017b, 2019), designing extremely high-concentration electrolyte to enhance the CE (Qiu et al., 2019a, 2019b; Ren et al., 2019; Yu et al., 2018), and constructing an artificial protective coating layer on the surface of Li metal anode (Lopez et al., 2018; Qian et al., 2019; Shen et al., 2019; Xie et al., 2019; Xu et al., 2018; Zhang et al., 2018b; Zhu et al., 2017). Nevertheless, the interphase layer is usually not strong enough to endure the severe mechanical stress induced by the infinite relative volume change of repetitive Li plating/stripping (Lin et al., 2017; Sun et al., 2019). Besides, building porous conductive hosts such as 3D porous metal foam and porous carbon matrix for accommodating Li is also

an effective strategy (Chi et al., 2017; Li et al., 2017; Wang et al., 2018a; Yang et al., 2018; Ye et al., 2017; Zhao et al., 2018). These porous hosts can not only restrain the generation of Li dendrites by lowering the local current density, but also reserve buffer spaces for Li deposition (Cheng et al., 2017; Qiu et al., 2019a, 2019b; Zhang et al., 2017a). But for most conductive hosts, Li nucleation sites are unpredictable and uncontrollable (Yue et al., 2019). Li deposition may occur toward the conductive separator-facing surface, which is called the "top-plating" problem, and result in the formation of dendrites. Thus, realizing selective Li nucleation and confining Li deposition within porous conductive hosts are critically important for suppressing dendrite growth.

Recently, Cui et al. reported that Li nucleation would occur preferentially on the surface of noble metals (Ag and Au) owing to the distinction of Li nucleation overpotential between the substrate and noble metals (Yan et al., 2016). Therefore, introducing Ag or Au into porous hosts have been investigated to regulate Li deposition behavior. The examples include Janus Au nanoparticle-modified carbon paper, Au nanoparticles pillared reduced graphene oxide, Ag nanoparticles anchored on the carbon nanofibers, Ag nanocrystals anchored on graphene, and three-dimensional graphene/Ag aerogel (Hong et al., 2019; Pu et al., 2018; Wang et al., 2018b; Yang et al., 2017, 2019b; Zhang et al., 2018a). However, most of these strategies are time consuming and complicated in process, and the high cost of noble metals also severely constrains the widespread practical application.

Herein, Ni macropore arrays on the Cu foil substrate were designed and prepared through a facile hydrogen bubble dynamic template-assisted electrodeposition method, which can be directly used as the functional current collector for Li-metal anode. In the Ni macropore array electrode, electric field distribution is entirely distinguishable from the conventional planar electrode. Numerical simulation results demonstrate that Li nucleation and growth can be well confined within conductive Ni macropores. The stable Li plating/stripping process can be well confined within conductive Ni macropores, eliminating the formation of Li dendrites effectively. As a result, the Ni macropore array electrode exhibits much-enhanced CE and remarkable cycling stability.

RESULTS AND DISCUSSION

Characterization and Numerical Simulation

We design a facile, scalable, and one-step electrodeposition method to fabricate the Ni macropore array electrode (Figure 1A). Owing to the high cathodic current ($3.0 \, A \, cm^{-2}$) applied on the substrate, the deposition of metallic Ni is synchronously accompanied by the generation of a large amount of H_2 bubbles, originating from the reduction of H^+ ions in the electrolyte. Once an H_2 bubble is produced on the surface of the Cu foil substrate, Ni deposition in this area is suppressed and no Ni^{2+} ions are present. Because hydrogen overpotential on Cu is smaller than that on Ni in acidic media, H_2 bubbles tend to be formed on the surface of Cu substrate on the bottom rather than the freshly deposited Ni (Speight, 2004). Subsequently, H_2 bubbles act as the dynamic template and create a continuous gap from the Cu substrate to the interphase of electrolyte-air during the electrodeposition process. Thus, there is only growth of Ni in the gaps between H_2 bubbles, leading to the formation of Ni macropore arrays on the Cu substrate. The surface of Ni macropore arrays film is rather smooth, and no cracks and exposure of Cu substrate are observed (Figure 1B). Even being greatly bent, the Ni macropore arrays film does not fall off the substrate, revealing the strong adhesion force between the Cu substrate and electrodeposition film (Figure S1). To further confirm the chemical composition of the electrodeposition film, X-ray diffraction (XRD) patterns of the Ni macropore array electrode were also collected (Figure S2). Three weak peaks marked with blue rhombuses are indexed to the Cu foil substrate (JCPDS No. 04-0836). Other peaks are in good agreement with metallic Ni (JCPDS No. 04-0850), and no impurities are observed.

The detailed morphology and structure of the Ni macropore array electrode were further examined by scanning electron microscopy (SEM) (Figures 1C–1F). Cylinder-shaped pores with a diameter of 5–15 μm are uniformly distributed in the electrode (Figure 1C). And every integral tree-like "Ni wall" is composed of interconnected Ni nanoparticles ranging from ~200 to ~500 nm in size (inset in Figure 1C), and the abundant voids inside "Ni wall" ensure the complete wetting of electrolyte. We are convinced that the formation of macropores between the Ni walls are attributed to the dramatic H_2 bubble flow liberated from the Cu substrate, while nano-sized voids inside the Ni wall are created by small H_2 bubbles evolved from the freshly deposited Ni nanoparticles. As shown in the cross-sectional SEM images (Figures 1D–1F), the thickness of Ni macropore arrays is about 49.6 μm. The porosity (P) of Ni macropore arrays is calculated to be as
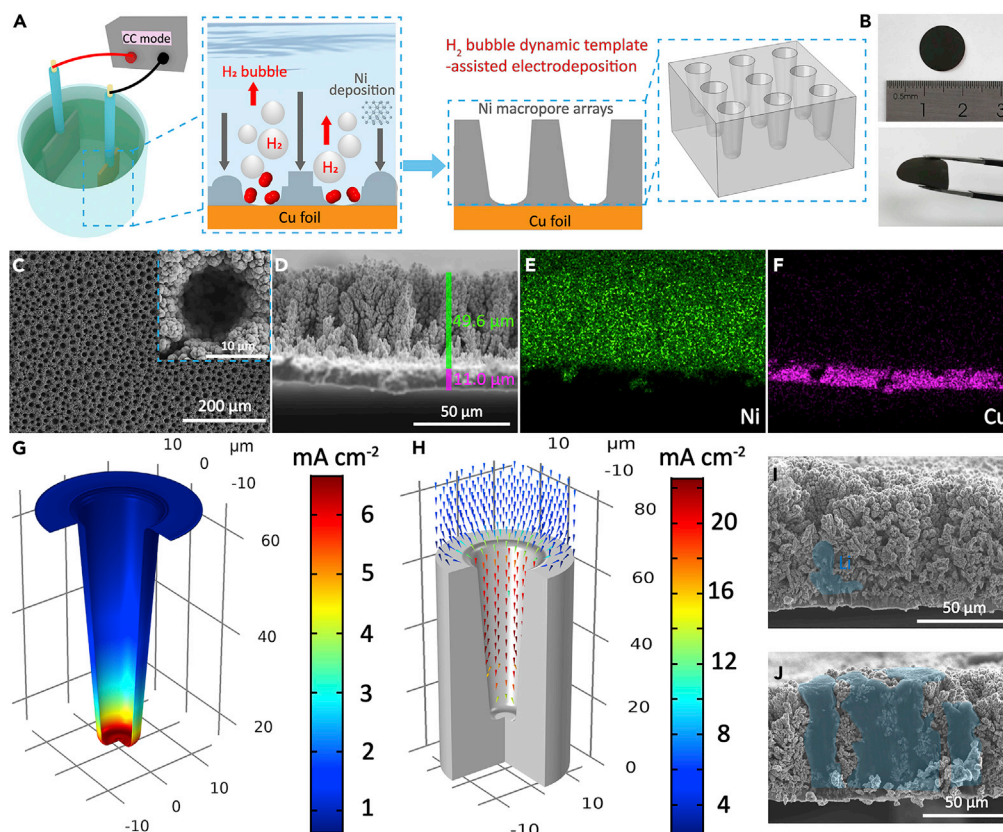
Figure 1. Characterization and Numerical Simualtion of the Ni Macropore Array Electrode

(A and B) (A) Schematic illustration of the preparation and (B) photographs of the Ni macropore array electrode.

(C) Surface SEM images of the Ni macropore array electrode.

(D–F) (D) Cross-sectional SEM image, (E) Ni and (F) Cu elemental mapping of the Ni macropore array electrode.

(G–J) (G and H) Numerical simulations of Li deposition behavior in Ni macropore arrays: (G) reaction current on the electrode/electrolyte interphase and (H) electric field distribution. Cross-sectional SEM images of the Ni macropore array electrode after Li plating at 0.5 mA cm^{-2} for (I) 1 h and (J) 6 h.

high as 78.9% by using the following equation ($P = 1 - \frac{V}{V_0}$), where V is the absolute compact volume and V_0 is the apparent volume. The relatively high porosity provides enough empty spaces for Li deposition inside Ni macropore arrays, which is in favor of relieving the structural stress during repeated Li plating/stripping.

This characteristic electrode structure is expected to exhibit unique electrochemical properties compared with the conventional planar electrode. Therefore, we first constructed the 3D model of Ni macropore arrays to simulate Li deposition behavior by using COMSOL software. Generally, Li deposition process can be divided into two steps of nucleation and growth, respectively. The reaction current on the electrode/electrolyte interphase (I_R) represents the electrochemical reaction rate, which is the decisive factor for Li nucleation (Figure 1G). As a certain current density is applied to the current collector, I_R located in different regions are varied deriving from the characteristic electrode structure. It is obvious that I_R on the inner surface of macropore arrays is much higher than that outside, meanwhile I_R inside macropore arrays increases with depth, which demonstrates that Li nucleation is predominantly initiated at the bottom of Ni macropores. After the nucleation, metallic Li continues to be deposited on the formed small Li particles. The growth direction and deposition velocity are mainly determined by the electric field distribution. As shown in Figure 1H, the electric field extends from the counter electrode to the bottom of Ni macropore arrays and the electric field value inside Ni macropores is much higher than that outside the electrode. The simulation results reveal that Li growth is preferentially confined within Ni macropores. In addition, the real-time simulation result has also been provided (Videos S1 and S2). Cross-sectional SEM images of the Ni macropore array electrode after Li plating at 0.5 mA cm^{-2} for 1 and 6 h (Figures 1I and 1J) corroborate the real-time simulation result that small Li particles are formed at the bottom and continue to grow within Ni
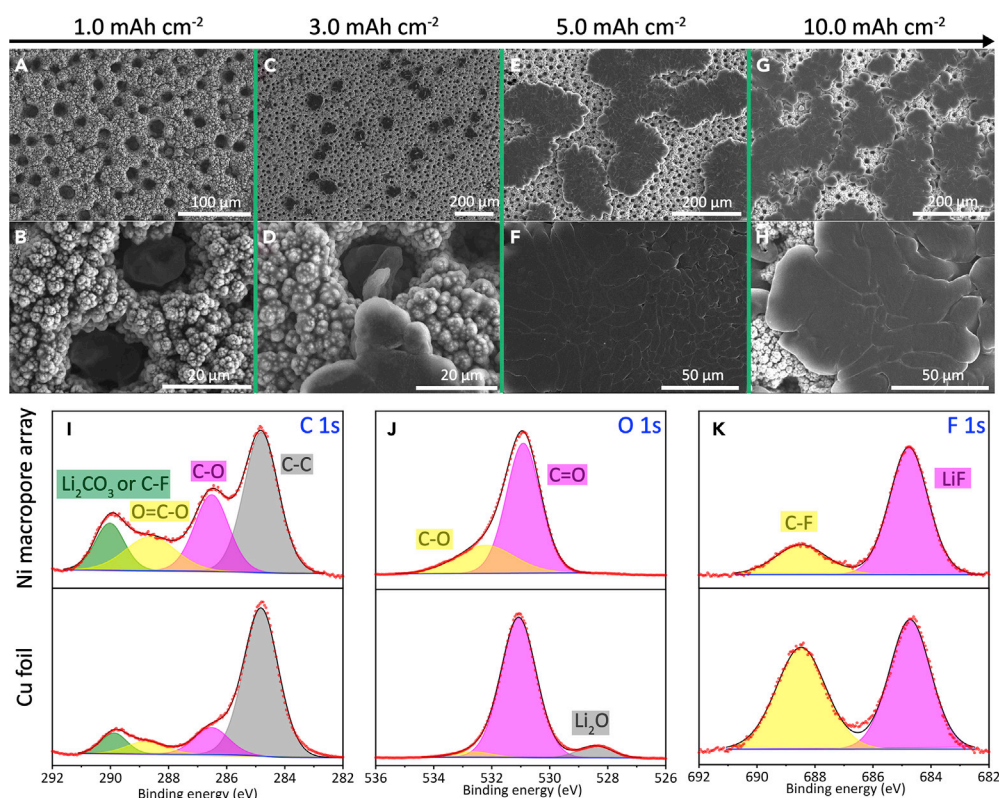
Figure 2. SEM Images and SEI Property of the Ni Macropore Array Electrode after Li Deposition

SEM images of the Ni macropore array electrode, after discharging to (A and B) 1.0, (C and D) 3.0, (E and F) 5.0, and (G and H) 10.0 mAh cm^{-2}. High-resolution XPS of (I) C 1s, (J) O 1s, and (K) F 1s of the SEI layer on the Ni macropore array and Cu foil electrodes after 10 cycles at 0.5 mA cm^{-2} with deposited capacity of 1.0 mAh cm^{-2} at Li plating state.

macropores with increasing plating duration. Given that the Li plating capacity is 5 mAh cm^{-2}, the gravimetric and volumetric specific capacities of the Li-Ni macropore array anode are calculated to be 537.6 mAh g^{-1} and 1,010.1 mAh cm^{-3}, respectively, which are superior than that of commercial graphite anode material (Table S1).

Li Plating Morphology and SEI Property

To further verify the numerical simulation results of Li deposition behavior, SEM images of the Ni macropore array electrode with different discharging capacities were obtained (Figures 2A–2H). The initial deposited Li of 1.0 mAh cm^{-2} is well accommodated inside Ni macropores (Figures 2A and 2B). When plating 3.0 mAh cm^{-2} capacity, Ni macropores are mainly filled with metallic Li particles (Figures 2C and 2D). The Ni macropore arrays structure can not only regulate Li nucleation/deposition behavior directionally but also enhance the electronic transport between Li particles and current collector. Therefore, with further plating, Li particles gradually spread on the surface (Figures 2E and 2F). Even the deposition amount of Li is increased to 10.0 mA cm^{-2}; no dendrites or mossy-like Li metal are observed (Figures 2G and 2H). In sharp contrast, obvious needle-like Li dendrites can be observed on the control Cu foil electrode with only 1.0 mAh cm^{-2} Li deposition (Figure S3). Based on the distinct Li deposition morphologies on the Ni macropore arrays and Cu foil electrodes, we deduce that the SEI layer formation may also be affected. To validate this hypothesis, X-ray photoelectron spectroscopy (XPS) measurements on both electrodes after 10 cycles is conducted (Figures 2I–2K). The C 1s spectra (Figure 2I) of both electrodes were fitted with four peaks assigned to Li$_2$CO$_3$ or C-F at 290.0 eV, O=C-O at 288.6 eV, C-O at 286.5 eV, and C-C at 284.8 eV, respectively (Shangguan et al., 2019). The higher relative ratio of oxygen-containing peaks for the Ni macropore array electrode indicates the larger amount of Li$_2$CO$_3$ and ROCO$_2$Li. Moreover, the O 1s spectra (Figure 2J) of the Ni macropore array electrode exhibit two peaks of C-O (532.2 eV) and C=O (530.9 eV). And no obvious Li$_2$O peak is observed, suggesting that the SEI layer formed on the Ni macropore array electrode is thicker than that grown on the Cu foil electrode (Yu et al., 2019). Since the generation of Li$_2$O is generally

considered to be resulted from the direct exposure of Li metal to the electrolyte without protection. It is worth noting that the SEI layer formed on the Ni macropore array electrode contains a higher content of F (4.45%) compared with that formed on the Cu foil electrode (2.94%) and the ratio of LiF to C-F is much enhanced (Figure 2K). According to previous reports, LiF is an electronic insulator with excellent electrochemical stability and plays a key role in restraining the formation of Li dendrites (Li et al., 2019). It is inferred that the enrichment of inorganic and organic lithium species, and LiF at the SEI layer formed on the surface of Ni macropore array electrode, is beneficial for the formation of stable and uniform SEI.

Stable Li Plating/Stripping Processes

To investigate the reversibility of Li plating/stripping on the Ni macropore arrays, we assembled coin cells with the Ni macropore array electrode as the working electrode and metal Li foil as the reference/counter electrode. The CE and lifespan are the two most significant indicators to evaluate the electrochemical performance of Li metal anodes. The CEs of the Ni macropore arrays and Cu foil electrodes at 0.5 mA cm^{-2} are shown in Figure 3A, which are measured by depositing 1.0 mAh cm^{-2} Li to the electrodes and stripping up to 1.0 V in each cycle. The Ni macropore array electrode maintains stable CEs of above 97% over 400 cycles at 0.5 mA cm^{-2}. In sharp contrast, the CE of Cu foil electrode shows a rapid decay after 120 cycles and eventually drops to nearly zero after 180 cycles owing to the continuous accumulation of Li dendrites and "dead Li." Even on increasing the current density, the Ni macropore array electrode still exhibits obviously better cycling stability and longer cycling life. High CEs of 97.6% and 96.5% can still be retained at enhanced current densities of 1.0 and 2.0 mA cm^{-2}, respectively (Figures 3B and 3C), and they are extraordinarily stable for at least 300 and 240 cycles at these enhanced current densities. In addition, the CEs of the Ni macropore array electrodes with higher areal specific capacities ranging from 3 to 5 mAh cm^{-2} at 2 mA cm^{-2} were also evaluated (Figure S4).

The typical voltage profiles of both electrodes at the current density of 0.5 mA cm^{-2} are presented in Figures 3D and 3E. The charge-discharge profiles of the Cu foil electrode fluctuate dramatically after only 150 cycles (Figure 3D). However, the profiles of the Ni macropore array electrode are almost identical for as long as 400 cycles (Figure 3E), revealing the excellent cycling stability. Moreover, the Ni macropore array electrode can retain a low and stable voltage hysteresis of ~26 mV during different cycle numbers (Figure 3F), demonstrating the negligible polarization effects. In comparison, the voltage hysteresis of Cu foil electrode is higher than ~30 mV all along and increased rapidly after 120 cycles, which is consistent with the sudden decay of CEs in Figure 4A. To further confirm the superior plating/stripping reversibility of the Ni macropore array electrode, symmetric cells were also fabricated and cycled with a fixed discharging/charging capacity of 1.0 mAh cm^{-2} at 0.5 mA cm^{-2} (Figure 3G). The Li-Cu foil symmetric cell displays the constant rising trend of voltage hysteresis (>40 mV) and failed after only 70 h, resulting from the growth of Li dendrites. In contrast, the Li-Ni macropore array electrode owns a small overpotential (~21 mV) without voltage fluctuation in the long duration of 800 h.

Mechanism Investigation

The stability mechanism of the Ni macropore array electrode was further clarified by *ex situ* SEM imaging (Figures 4A–4D). A thin polymer-like SEI film can be distinctly observed on the surface of Ni nanoparticles after cycling (Figure S5). As can be seen, bulk Li particles with no dendrites are observed at the bottom of Ni macropore arrays after 50 and 100 cycles at the Li deposition state (Figures 4A and 4C), indicating that the controllable Li nucleation and growth can be achieved during long-term cycling. For the Ni macropore array electrode after 50 and 100 cycles at the Li stripping state (Figures 4B and 4D), the surface is quite smooth and no significant "dead Li" is observed. Moreover, the Ni macropore arrays structure is maintained well without any damages, demonstrating the remarkable structural stability during repeated Li plating/stripping. Besides, the highly porous Ni macropore arrays structure can also effectively relieve the volume change and may be beneficial to retain the stability of SEI film during cycling. Therefore, *in situ* Raman spectra of the Ni macropore array electrode were obtained (Figure 4E). The peak at ~740 cm^{-1} (bending mode from CF$_3$) becomes more obvious during the initial Li deposition process, revealing the decomposition of LiTFSI in the electrolyte to form SEI film on the electrode surface. Moreover, the peak intensity is maintained strongly during these two cycles, demonstrating the superior stability of SEI film. The properties of electrolyte/electrode interface were further investigated by EIS (Figure S6). R$_s$ and R$_{ct}$ represent the electrolyte resistance and charge-transfer resistance, respectively. As shown in Table S2, R$_{ct}$ of the Ni macropore array electrode (9.06 Ω) is much smaller than that of Cu foil electrode (22.7 Ω), indicating the improved charge-transfer process. In brief, Li deposition behavior onto the Ni macropore
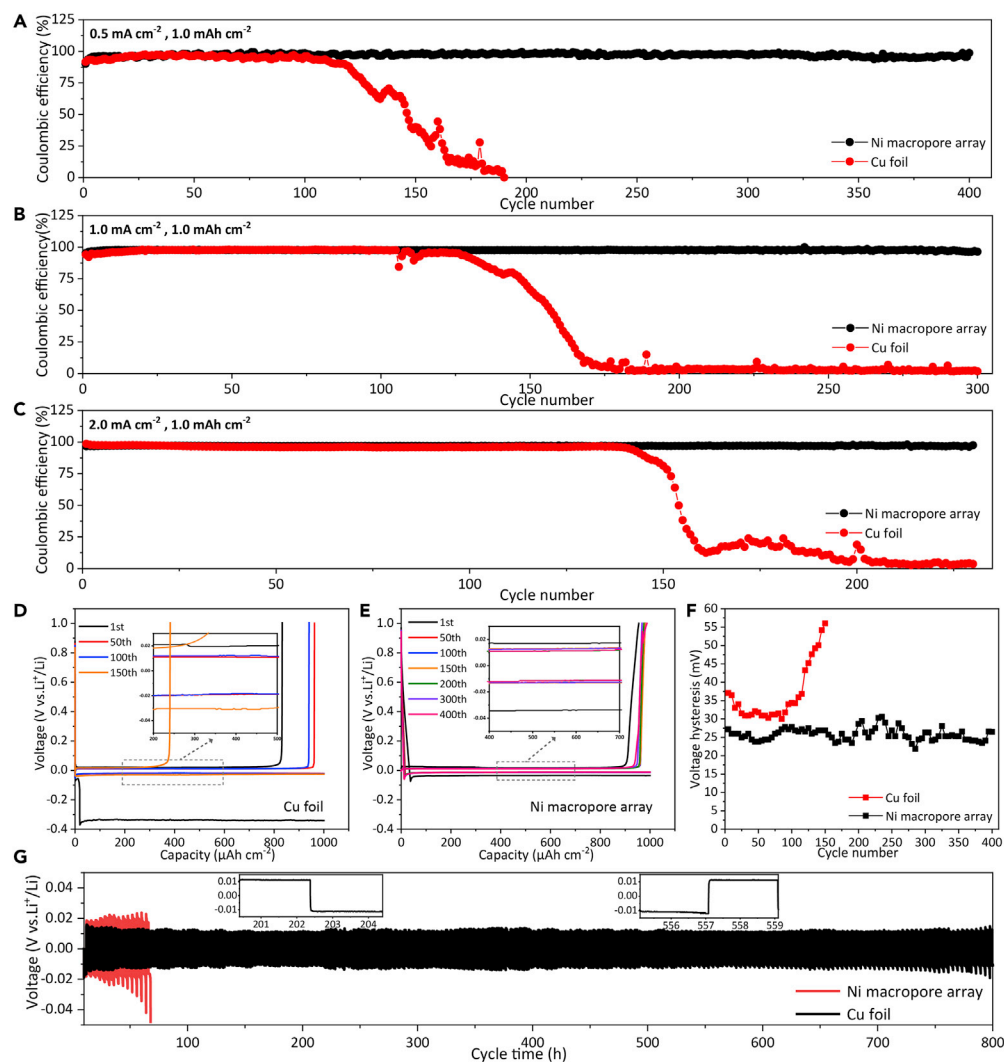
Figure 3. Electrochemical Performance of Half Cells

(A–C) Comparison of Coulombic efficiency (CE) of the Ni macropore array and Cu foil electrodes with a constant lithiation capacity of 1.0 mAh cm^{-2} at different current densities: (A) 0.5, (B) 1.0, and (C) 2.0 mA cm^{-2}.

(D) Voltage profiles of the Cu foil electrode at 0.5 mA cm^{-2}.

(E) Voltage profiles of the Ni macropore array electrode at 0.5 mA cm^{-2}.

(F) Voltage hysteresis of the Ni macropore array and Cu foil electrodes at 0.5 mA cm^{-2}.

(G) Galvanostatic voltage-time curves for symmetrical cells of the Ni macropore array and Cu foil electrodes with a fixed plating/stripping capacity of 1.0 mAh cm^{-2} at 0.5 mA cm^{-2} (inset is the detailed voltage profiles).

arrays is illustrated in Figure 4F. Owing to the regulated electric field distribution, Li nucleation may be initialized from the bottom of Ni macropore arrays. With the increment of plating capacity, metallic Li is first filled within these Ni macropores and spread over the surface gradually. The outstanding structural integrity and stable electrode/electrolyte interface benefiting from the specific Ni macropore arrays structure are proved to make a significant contribution to the excellent electrochemical performance.

Electrochemical Performance of Full Cells

To further verify the feasibility of the Ni macropore arrays design, full cells using LiFePO$_4$ as the cathode coupled with Li-Ni macropore array and Li-Cu foil electrodes as the anode have been assembled. As shown in Figure 5A, the LiFePO$_4$ ‖ Li-Ni macropore array battery exhibits average discharge capacities of 155.3, 148.5, 135.2, 118.3, 104.9, 92.2, 79.2, 68.7, 57.0, and 44.4 mAh g^{-1} when the current density is increased from 0.1 to 4 C step by step. Although the capacity of the LiFePO$_4$ ‖ Li-Cu foil battery is close to that of
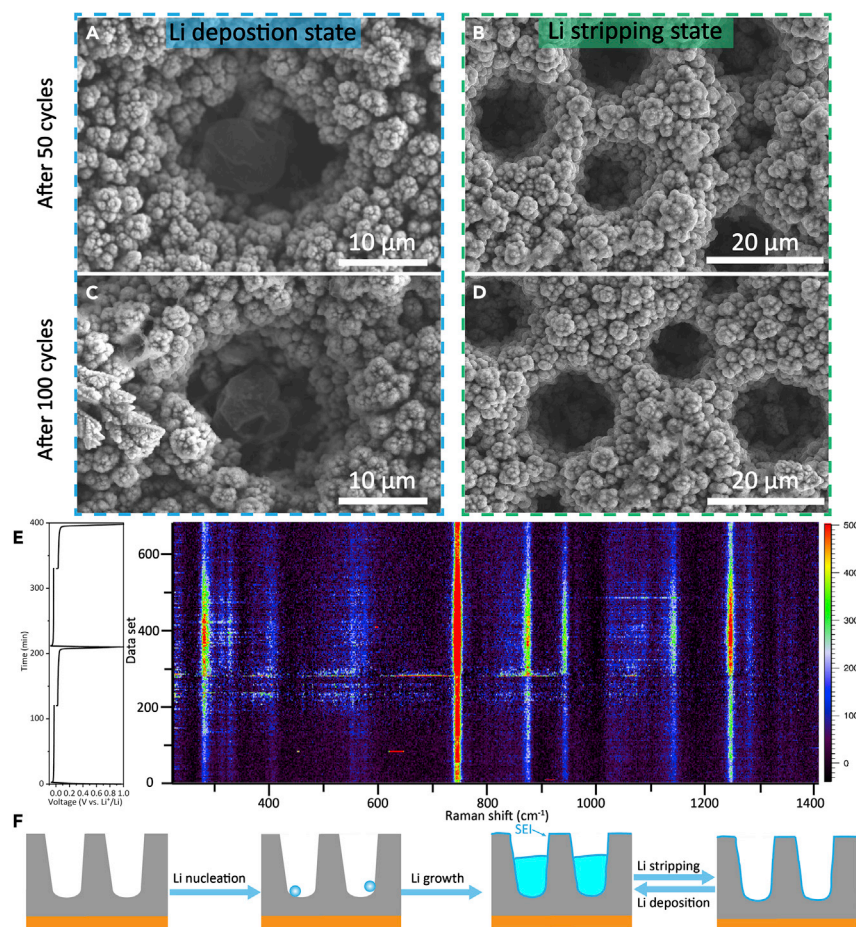
Figure 4. Morphology Variations and In Situ Raman Spectra of the Ni Macropore Array Electrode during Cycling

(A–D) Morphology variations of the Ni macropore array electrode after different cycles. The cells are tested at 0.5 mA cm^{-2} with a capacity of 1.0 mAh cm^{-2}: (A and B) SEM images of the Ni macropore array electrode after 50 cycles at the Li deposition state and Li stripping state, respectively. (C and D) SEM images of the Ni macropore array electrode after 100 cycles at the Li deposition state and Li stripping state, respectively.

(E) *In situ* Raman spectra of the Ni macropore array electrode at 0.5 mA cm^{-2} with a capacity of 1.0 mAh cm^{-2}.

(F) Schematic illustration of Li deposition/stripping processes in the Ni macropore array electrode.

the full cell with a Li-Ni macropore arrays anode during 0.1 and 0.2 C cycling, the capacity rapidly decreases to almost zero at only 2.5 C. The superior rate capability of the full cell with a Li-Ni macropore array anode may be attributed to the smaller polarization (Figures 5B and 5C). More details of the voltage hysteresis of both full cells at various current densities are shown in Figure S7. It can be clearly seen that the LiFePO$_4$ || Li-Ni macropore array battery shows a much lower voltage hysteresis than that of the LiFePO$_4$ || Li-Cu foil battery, especially during high rate cycling. Moreover, the LiFePO$_4$ || Li-Ni macropore array battery presents a high capacity of 90.3 mAh g^{-1} over 700 cycles at 1 C (Figure 5D), indicating the superior cycling stability, whereas, the LiFePO$_4$ || Li-Cu foil battery exhibits quick capacity after 400 cycles and only a limited capacity of 20 mAh g^{-1} can be retained after 500 cycles.

Conclusion

In summary, we have demonstrated Ni macropore arrays on the Cu foil substrate as a functional host for Li deposition. Numerical simulation results and SEM images after cycling indicate that Li nucleation and deposition processes prefer to occur at the bottom of Ni macropore arrays owing to the regulated electric field distribution inside the electrode. The Ni macropore arrays structure can not only enhance the electrons transport between Li particles and current collector but also provide buffer spaces for accommodating Li deposition. Consequently, stable Li plating/stripping with small hysteresis confined in the Ni
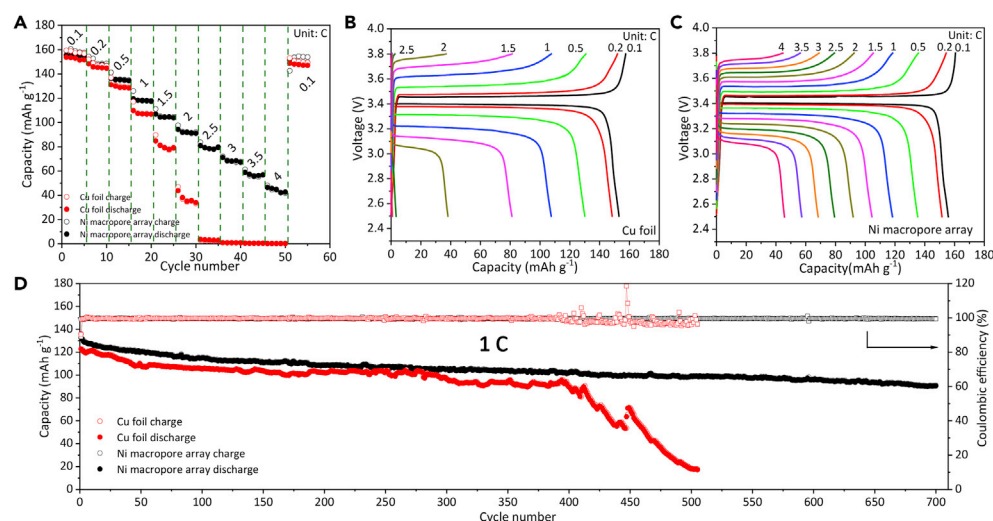
Figure 5. Rate Performance and Long-term Cycling Performance of Full Cells

Electrochemical performance of full cells with Li-Ni macropore array anode and Li-Cu foil anode against LiFePO$_4$ cathode: (A) Rate performance of both full batteries. (B) Typical voltage profiles of the LiFePO$_4$ ‖ Li-Cu foil battery. (C)Typical voltage profiles of the LiFePO$_4$ ‖ Li-Ni macropore array battery. (D) Cycling performances of both full batteries at 1 C.

macropore arrays have been achieved. As a result, a high CE of above 97% can be maintained for over 400 cycles with a capacity of 1.0 mAh cm^{-2}. The rationally designed Ni macropore array electrode fabricated by the rapid and scalable electrochemical deposition method presents a promising route to long-life and high-safety Li metal anodes for high-energy-density Li metal batteries.

Limitations of the Study

For the current study, the mass of the Cu foil substrate with the thickness of ~11 μm is ~9.3 mg cm^{-1}, which inevitably increases the total weight of batteries. It is expected that a thinner Cu foil or ultrathin polymeric backbone on which a copper thin film is deposited may be used to increase the energy density of the electrode. In addition, future work focusing on the modification of electrolytes is needed to further enhance the Coulombic efficiency to meet the requirements of commercial lithium ion batteries.

METHODS

All methods can be found in the accompanying Transparent Methods supplemental file.

DATA AND CODE AVAILABILITY

The data that support the findings of this study are available from the corresponding author upon reasonable request.

SUPPLEMENTAL INFORMATION

Supplemental Information can be found online at https://doi.org/10.1016/j.isci.2020.101089.

AUTHOR CONTRIBUTIONS

Y.Y. and C.C.L. conceived the idea and designed the experiments. Y.Y. and J.X. carried out the electrode preparation and electrochemical experiments. Y.Y., J.Z., and W.H. wrote the paper and analyzed the results. C.L. performed the COMSOL numerical simulation. D.C. carried out the *in situ* Raman measurement. Y.Z. and H.G. conducted the material characterization. All authors read and approved the final manuscript.

REFERENCES

Cheng, X.-B., Zhang, R., Zhao, C.-Z., and Zhang, Q. (2017). Toward safe lithium metal anode in rechargeable batteries: a review. Chem. Rev. *117*, 10403–10473.

Chi, S.-S., Liu, Y., Song, W.-L., Fan, L.-Z., and Zhang, Q. (2017). Prestoring lithium into stable 3D nickel foam host as dendrite-free lithium metal anode. Adv. Funct. Mater. *27*, 1700348.

Hong, B., Fan, H.L., Cheng, X.B., Yan, X.L., Hong, S., Dong, Q.Y., Gao, C.H., Zhang, Z., Lai, Y.Q., and Zhang, Q. (2019). Spatially uniform deposition of lithium metal in 3D Janus hosts. Energy Storage Mater. *16*, 259–266.

Li, M., Lu, J., Chen, Z., and Amine, K. (2018). 30 Years of lithium-ion batteries. Adv. Mater. *30*, 1800561.

Li, Q., Zhu, S., and Lu, Y. (2017). 3D porous Cu current collector/Li-metal composite anode for stable lithium-metal batteries. Adv. Funct. Mater. *27*, 1606422.

Li, T., Zhang, X.-Q., Shi, P., and Zhang, Q. (2019). Fluorinated solid-electrolyte interphase in high-voltage lithium metal batteries. Joule *3*, 2647–2661.

Liang, Z., Lin, D., Zhao, J., Lu, Z., Liu, Y., Liu, C., Lu, Y., Wang, H., Yan, K., Tao, X., et al. (2016). Composite lithium metal anode by melt infusion of lithium into a 3D conducting scaffold with lithiophilic coating. Proc. Natl. Acad. Sci. U S A *113*, 2862–2867.

Lin, D., Liu, Y., and Cui, Y. (2017). Reviving the lithium metal anode for high-energy batteries. Nat. Nanotechnol. *12*, 194–206.

Lopez, J., Pei, A., Oh, J.Y., Wang, G.-J.N., Cui, Y., and Bao, Z. (2018). Effects of polymer coatings on electrodeposited lithium metal. J. Am. Chem. Soc. *140*, 11735–11744.

McDowell, M.T., Lee, S.W., Nix, W.D., and Cui, Y. (2013). 25th anniversary article: understanding the lithiation of silicon and other alloying anodes for lithium-ion batteries. Adv. Mater. *25*, 4966–4985.

Pu, J., Li, J.C., Shen, Z.H., Zhong, C.L., Liu, J.Y., Ma, H.X., Zhu, J., Zhang, H.G., and Braun, P.V. (2018). Interlayer lithium plating in Au nanoparticles pillared reduced graphene oxide for lithium metal anodes. Adv. Funct. Mater. *28*, 1804133.

Qian, J., Li, Y., Zhang, M., Luo, R., Wang, F., Ye, Y., Xing, Y., Li, W., Qu, W., Wang, L., et al. (2019). Protecting lithium/sodium metal anode with metal-organic framework based compact and robust shield. Nano Energy *60*, 866–874.

Qiu, F., Li, X., Deng, H., Wang, D., Mu, X., He, P., and Zhou, H. (2019a). A concentrated ternary-salts electrolyte for high reversible Li metal battery with slight excess Li. Adv. Energy Mater. *9*, 1803372.

Qiu, H., Tang, T., Asif, M., Huang, X., and Hou, Y. (2019b). 3D porous Cu current collectors derived by hydrogen bubble dynamic template for enhanced Li metal anode performance. Adv. Funct. Mater. *29*, 1808468.

Ren, X., Zou, L., Jiao, S., Mei, D., Engelhard, M.H., Li, Q., Lee, H., Niu, C., Adams, B.D., Wang, C., et al. (2019). High-concentration ether electrolytes for stable high-voltage lithium metal batteries. ACS Energy Lett. *4*, 896–902.

Shangguan, X., Xu, G., Cui, Z., Wang, Q., Du, X., Chen, K., Huang, S., Jia, G., Li, F., Wang, X., et al. (2019). Additive-assisted novel dual-salt electrolyte addresses wide temperature operation of lithium-metal batteries. Small *15*, 1900269.

Shen, X., Cheng, X., Shi, P., Huang, J., Zhang, X., Yan, C., Li, T., and Zhang, Q. (2019). Lithium–matrix composite anode protected by a solid electrolyte layer for stable lithium metal batteries. J. Energy Chem. *37*, 29–34.

Speight, J.G. (2004). Lange's Handbook of Chemistry, 16th edition (McGraw-Hill Companies, Inc.), pp. 1–396.

Sun, C., Li, Y., Jin, J., Yang, J., and Wen, Z. (2019). ZnO nanoarray-modified nickel foam as a lithiophilic skeleton to regulate lithium deposition for lithium-metal batteries. J. Mater. Chem. A. *7*, 7752–7759.

Tarascon, J.M., and Armand, M. (2001). Issues and challenges facing rechargeable lithium batteries. Nature *414*, 359–367.

Wang, A., Zhang, X., Yang, Y.-W., Huang, J., Liu, X., and Luo, J. (2018a). Horizontal centripetal plating in the patterned voids of Li/graphene composites for stable lithium-metal anodes. Chem *4*, 2192–2200.

Wang, X., Pan, Z., Wu, Y., Xu, G., Zheng, X., Qiu, Y., Liu, M., Zhang, Y., and Li, W. (2018b). Reducing lithium deposition overpotential with silver nanocrystals anchored on graphene aerogel. Nanoscale *10*, 16562–16567.

Winter, M., Barnett, B., and Xu, K. (2018). Before Li ion batteries. Chem. Rev. *118*, 11433–11456.

Wu, H.P., Cao, Y., Geng, L.X., and Wang, C. (2017). In situ formation of stable interfacial coating for high performance lithium metal anodes. Chem. Mater. *29*, 3572–3579.

Xie, J., Jiang, Z., Jin, L., Han, Z., Hu, W., Zeng, Z., and Sun, Y. (2019). Facile generation of polymer-alloy hybrid layer towards dendrite-free lithium metal anode with improved moisture stability. Angew. Chem. *58*, 11374–11378.

Xu, R., Zhang, X.Q., Cheng, X.B., Peng, H.J., Zhao, C.Z., Yan, C., and Huang, J.Q. (2018). Artificial soft-rigid protective layer for dendrite-free lithium metal anode. Adv. Funct. Mater. *28*, 1870049.

Yan, K., Lu, Z.D., Lee, H.W., Xiong, F., Hsu, P.C., Li, Y.Z., Zhao, J., Chu, S., and Cui, Y. (2016). Selective deposition and stable encapsulation of lithium through heterogeneous seeded growth. Nat. Energy *1*, 8.

Yang, C., Yao, Y., He, S., Xie, H., Hitz, E., and Hu, L. (2017). Ultrafine silver nanoparticles for seeded lithium deposition toward stable lithium metal anode. Adv. Mater. *29*, 1702714.

Yang, Y., Xiong, J., Lai, S., Zhou, R., Zhao, M., Geng, H., Zhang, Y., Fang, Y., Li, C., and Zhao, J. (2019a). Vinyl ethylene carbonate as an effective SEI-forming additive in carbonate-based electrolyte for lithium-metal anodes. ACS Appl. Mater. Interfaces *11*, 6118–6125.

Yang, Y., Xiong, J., Zeng, J., Huang, J., and Zhao, J. (2018). VGCF 3D conducting host coating on glass fiber filters for lithium metal anodes. Chem. Commun. *54*, 1178–1181.

Yang, Y., Zhao, M., Geng, H., Zhang, Y., Fang, Y., Li, C., and Zhao, J. (2019b). Three-dimensional graphene/Ag aerogel for durable and stable Li metal anodes in carbonate-based electrolytes. Chem. Eur. J. *25*, 5036–5042.

Ye, H., Xin, S., Yin, Y.-X., and Guo, Y.-G. (2017). Advanced porous carbon materials for high-efficient lithium metal anodes. Adv. Energy Mater. *23*, 1700530.

Yu, L., Chen, S., Lee, H., Zhang, L., Engelhard, M.H., Li, Q., Jiao, S., Liu, J., Xu, W., and Zhang, J.-G. (2018). A localized high-concentration electrolyte with optimized solvents and lithium difluoro(oxalate)borate additive for stable lithium metal batteries. ACS Energy Lett. *3*, 2059–2067.

Yu, S.-H., Huang, X., Brock, J.D., and Abruna, H.D. (2019). Regulating key variables and visualizing lithium dendrite growth: an operando X-ray study. J. Am. Chem. Soc. *141*, 8441–8449.

Yue, X.-Y., Li, X.-L., Wang, W.-W., Chen, D., Qiu, Q.-Q., Wang, Q.-C., Wu, X.-J., Fu, Z.-W., Shadike, Z., Yang, X.-Q., et al. (2019). Wettable carbon felt framework for high loading Li-metal composite anode. Nano Energy *60*, 257–266.

Zhang, C., Huang, Z., Lv, W., Yun, Q., Kang, F., and Yang, Q.-H. (2017a). Carbon enables the practical use of lithium metal in a battery. Carbon *123*, 744–755.

Zhang, Q., Wang, K., Wang, X., Zhong, Y., Liu, M., Liu, X., Xu, K., Fan, W., Yu, L., and Li, W. (2019). Lithium Bis(oxalate)borate reinforces the interphase on Li-metal anodes. ACS Appl. Mater. Interfaces *11*, 20854–20863.

Zhang, R., Chen, X., Shen, X., Zhang, X.-Q., Chen, X.-R., Cheng, X.-B., Yan, C., Zhao, C.-Z., and Zhang, Q. (2018a). Coralloid carbon fiber-based composite lithium anode for robust lithium metal batteries. Joule *2*, 764–777.

Zhang, S.-J., Gao, Z.-G., Wang, W.-W., Lu, Y.-Q., Deng, Y.-P., You, J.-H., Li, J.-T., Zhou, Y., Huang, L., Zhou, X.-D., et al. (2018b). A natural biopolymer film as a robust protective layer to effectively stabilize lithium-metal anodes. Small *14*, 1801054.

Zhang, X.-Q., Cheng, X.-B., Chen, X., Yan, C., and Zhang, Q. (2017b). Fluoroethylene carbonate additives to render uniform Li deposits in lithium metal batteries. Adv. Funct. Mater. *27*, 1605989.

Zhao, H., Lei, D., He, Y.-B., Yuan, Y., Yun, Q., Ni, B., Lv, W., Li, B., Yang, Q.-H., Kang, F., et al. (2018). Compact 3D copper with uniform porous structure derived by electrochemical dealloying as dendrite-free lithium metal anode current collector. Adv. Energy Mater. *8*, 1800266.

Zhu, B., Jin, Y., Hu, X., Zheng, Q., Zhang, S., Wang, Q., and Zhu, J. (2017). Poly(dimethylsiloxane) thin film as a stable interfacial layer for high-performance lithium-metal battery anodes. Adv. Mater. *29*, 1603755.

Supplemental Information

Uniform Li Plating/Stripping within Ni Macropore

Arrays Enabled by Regulated Electric Field

Distribution for Ultra-Stable Li-Metal Anodes

Yang Yang, Jinfei Xiao, Chaoyue Liu, Dongjiang Chen, Hongbo Geng, Yufei Zhang, Jinbao Zhao, Cheng Chao Li, and Weidong He

Uniform Li plating/stripping within Ni macropore arrays enabled by regulated electric field distribution for ultra-stable Li-metal anodes

Yang Yang[1], Jinfei Xiao[1], Chaoyue Liu[2], Dongjiang Chen[3], Hongbo Geng[1], Yufei Zhang[1], Jinbao Zhao[2], Cheng Chao Li[1,4,*], Weidong He[3,*]

[1]School of Chemical Engineering and Light Industry, Guangdong University of Technology, Guangzhou 510006, China

[2]State Key Lab of Physical Chemistry of Solid Surfaces, State-Province Joint Engineering Laboratory of Power Source Technology for New Energy Vehicle, College of Chemistry and Chemical Engineering, Xiamen University, Xiamen, 361005, China

[3]National Key Laboratory of Science and Technology on Advanced Composites in Special Environments Center for Composite Materials and Structures, Harbin Institute of Technology, Harbin 150080, China

[4]Lead Contact

*Correspondence: licc@gdut.edu.cn (C. C. L.); weidong.he@hit.edu.cn (W. H.)

TRANSPARENT METHODS

Fabrication of Ni macropore arrays

Ni macropore arrays on a Cu substrate were prepared by the electrochemical deposition method(Li et al., 2007; Zhang et al., 2012). Prior to use, a piece of Cu foil was thoroughly rinsed with acetone, ethanol and deionized water in sequence. Then the Cu foil was masked by the insulating Kapton film, leaving an exposed area of 2.25 cm^2 (1.5 cm $\times$ 1.5 cm). The treated Cu foil and carbon paper (4.0 cm $\times$ 5.0 cm) were used as the working electrode and counter electrode, respectively. The electrolyte was 2.0 M NH_4Cl and 0.1 M $NiCl_2 \cdot 6H_2O$ aqueous solution. The electrodeposition process was performed at a constant current density of 3.0 A cm^{-2} for the duration of 60 seconds with vigorous stirring. The resulting brown films on the Cu foil were immersed in 500 mL deionized water to remove the residual electrolyte, and dried overnight at 60 °C in the vacuum oven.

Characterizations

X-ray diffraction (XRD) patterns were recorded on the Miniflex 600 diffractormeter (Rigaku) with Cu Kα radiation. The morphology of samples was characterized by using a scanning electron microscope (SEM, S-3400N, Hitachi). Prior to the analyses, the electrodes after cycling were disassembled from the electrochemical cells, rinsed three times with DME (1,2-dimethoxyethane) solvent, and dried in the grove box.

Numerical simulation

The model is constructed in COMSOL Multiphysics framework. In order to simulate the deposition process which involves large shape distortion, the level set method is chosen to

track the moving boundary of lithium metal surface. General PDE module is used to describe the electrochemical system.

Level set method use a status variable ξ to distinguish different phases. ξ equals to 0 and 1 in solid and liquid phases respectively. The following equation is solved to track the moving interphase:

$$\frac{\partial \xi}{\partial t} + \boldsymbol{u} \cdot \nabla \xi = \gamma \nabla \cdot (\epsilon \nabla \xi - \xi(1-\xi)\frac{\nabla \xi}{|\nabla \xi|})$$

γ determines the amount of initialization. ϵ determines the thickness of transition region. $\boldsymbol{u}$ is the velocity field which is related to local current density through molar volume of lithium metal:

$$\boldsymbol{u} = \frac{i_{loc}V_m}{F} \cdot \frac{\nabla \xi}{|\nabla \xi|}$$

F is Faraday's constant. $\frac{\nabla \xi}{|\nabla \xi|}$ is the normal vector at the interphase. The molar volume V_m is 12.998 cm^3 mol^{-1}.

The current density in liquid and solid phase are described by following equations:

$$i_l = -\sigma_{l,eff}\nabla\phi_l + \left(\frac{2\sigma_{l,eff}RT}{F}\right)\left(1 + \frac{\partial lnf}{\partial lnc_l}\right)(1 - t_+)\nabla lnc_l$$

$$i_s = -\sigma_{s,eff}\nabla\phi_s$$

Here $\frac{\partial lnf}{\partial lnc_l} = \left(0.601 - 0.24c_l^{0.5} + 0.893(1 - 0.0052(T - 294))c_l^{1.5}\right)(1 - t_+^0)^{-1} - 1$ accounts for the activity dependence. The transfer coefficient t_+=0.38. In order to combine PDEs with level set method, statistic electro potential in both phases has to be continuous in the whole model. Thus, the electronic conductivities are modified by status function ξ as $\sigma_{l,eff} = \sigma_l\xi + \sigma_0(1 - \xi)$ and $\sigma_{s,eff} = \sigma_0\xi + \sigma_s(1 - \xi)$. σ_0 is set to 1×10^{-8} S m^{-1}.

The controlling equations of charge conservation in both phases are written as followings:

$$\nabla \cdot i_l = i_{loc}\delta$$

$$\nabla \cdot i_s = -i_{loc}\delta$$

Here, $\delta = 6\xi(1-\xi)\left|\frac{\nabla\xi}{|\nabla\xi|}\right|$ is a function whose integration over 0 to 1 is 1 and is nonzero only in the interphase region. Local current density arising from overpotential η is defined by Butler-Volmer equation herein as:

$$i_{loc} = Fkc_l^{0.5}\left(exp\left(\frac{0.5F\eta}{RT}\right) - exp\left(-\frac{0.5F\eta}{RT}\right)\right)$$

$k=1.147\times10^{-4}$ mol m^{-2} s^{-1} is the reaction rate constant.

The mass conservation in liquid phase is given by:

$$\xi\frac{\partial c_l}{\partial t} - D_l c_l + \frac{i_l t_+}{F} = \frac{i_{loc}\delta}{F}$$

In which the electrolyte diffusivity $D_l = 10^{-4} \times 10^{-4.43-\frac{54}{T-229-5c_l}-0.22c_l}$ (Sturm et al., 2019).

Electrochemical measurements

Electrochemical measurements were performed by using CR-2016 type coin cells. The Ni macropore array electrode was punched into discs with the diameter of 1.2 cm, and used as the working electrode. A metallic Li foil with the diameter of 1.6 cm was used as the reference and counter electrode. Lithium bis(trifluoromethanesulfonyl)-imide (LiTFSI, 1.0 M) in 1,3-dioxolane (DOL) and 1,2-dimethoxyethane (DME) (volume ratio = 1/1) with 1 wt% LiNO$_3$ as additive was used as the electrolyte, and the amount of electrolyte used in the assembly of half cells was fixed at 0.089 mL mAh^{-1} when the Li plating capacity was

1 mAh cm^{-2}. Celgard 2400 microporous polypropylene membrane was employed as the separator. Before Li plating, the half cells were primarily activated for 5 cycles at 0.5 mA cm^{-2} between 0 and 1.0 V (vs. Li$^+$/Li) to stabilize SEI and remove surface contaminations. For the test of CEs, the plating process was set to a certain area capacity at a constant area current density, and the stripping process was charging to 1.0 V. For the fabrication of symmetric batteries, 4.0 mAh cm^{-2} of Li was predeposited onto the Ni macropore array electrodes, and two as-prepared electrodes were assembled together into the CR-2032 type coin cells. Then a fixed capacity of 1 mAh cm^{-2} was applied during repeated discharge/charge at 0.5 mA cm^{-2} to obtain the time-voltage profiles. Electrochemical impedance spectroscopy (EIS) was collected with the frequency range of 100 kHz ~ 0.1 Hz by using the electrochemical workstation (Interface 1010B, Gamry).

The full cells were assembled by using 4 mAh cm^{-2} of deposited Li on Ni macropore array electrode as the anode, and LiFePO$_4$ electrode as the cathode. For the preparation of LiFePO$_4$ electrode, 80 wt% commercial LiFePO$_4$ (Hefei Guoxuan High-tech Power Energy Co., Ltd), 10 wt% super P and 10 wt% PVDF (polyvinylidene fluoride) was thoroughly mixed in NMP (N-methylpyrrolidine) solvent. The slurry was coated onto the Al foil by using an automatic film coating machine, and dried a vacuum oven at 80 °C for 12 h. The mass loading of active materials in LiFePO$_4$ electrodes is approximately 4.3 ~ 4.8 mg cm^{-2}. All the electrochemical properties were measured at the room temperature.
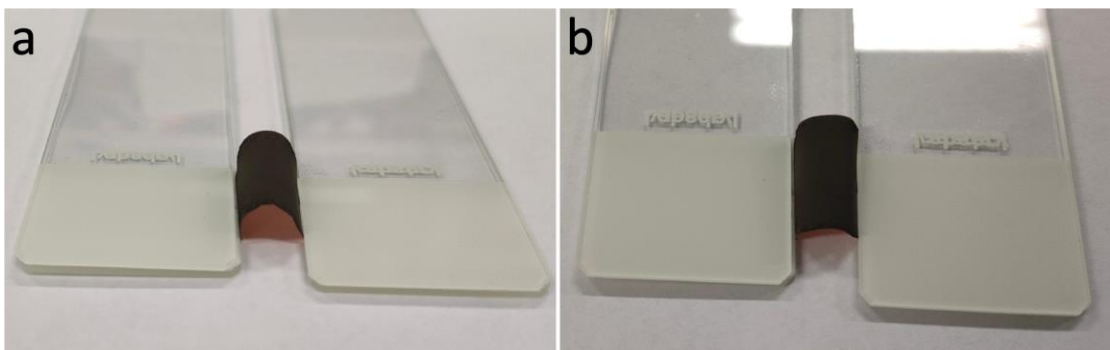
Figure S1. Photographs of the bending test of the Ni macropore array electrode. Related to
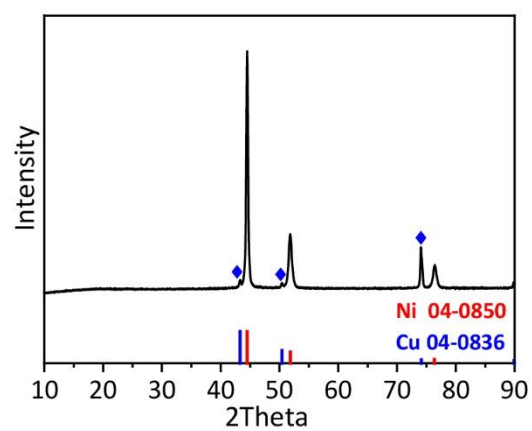
Figure 1.

Figure S2. XRD patterns of the Ni macropore array electrode. Related to Figure 1.

Table S1. The comparison of graphite and Li-Ni macropore array anode in terms of gravimetric specific capacity and volumetric specific capacity. The specific discharge capacity of commercial graphite (Alladin) was evaluated to be ~334.7 mAh g^{-1} at 0.5 C, and the tap density was measured to be approximately 0.71 g cm^{-3}. Related to Figure 1.

Sample	Gravimetric specific capacity (mAh g^{-1})	Volumetric specific capacity (mAh cm^{-3})
Graphite	334.7	237.6
Li-Ni macropore array anode	537.6	1010.1
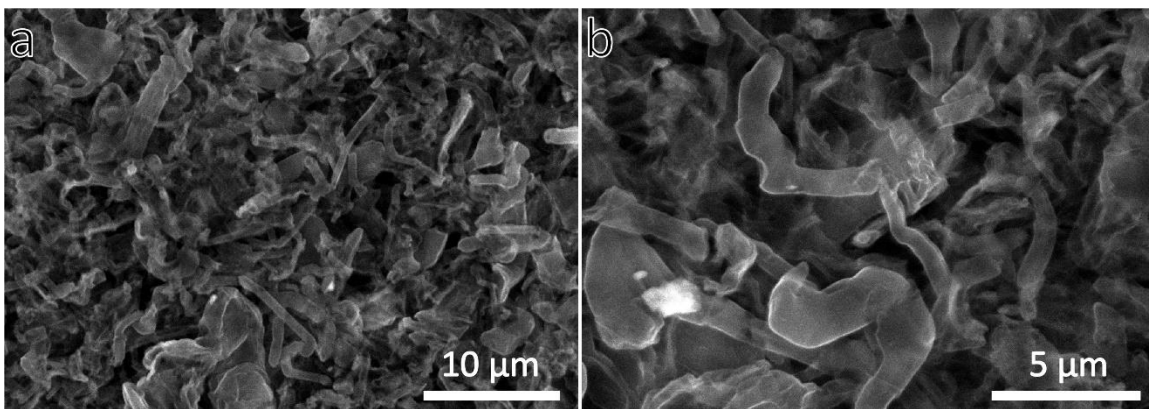
Figure S3. SEM images of the Cu foil electrode after discharging to 1.0 mAh cm^{-2} at 0.5 mA cm^{-2}. Related to Figure 2.
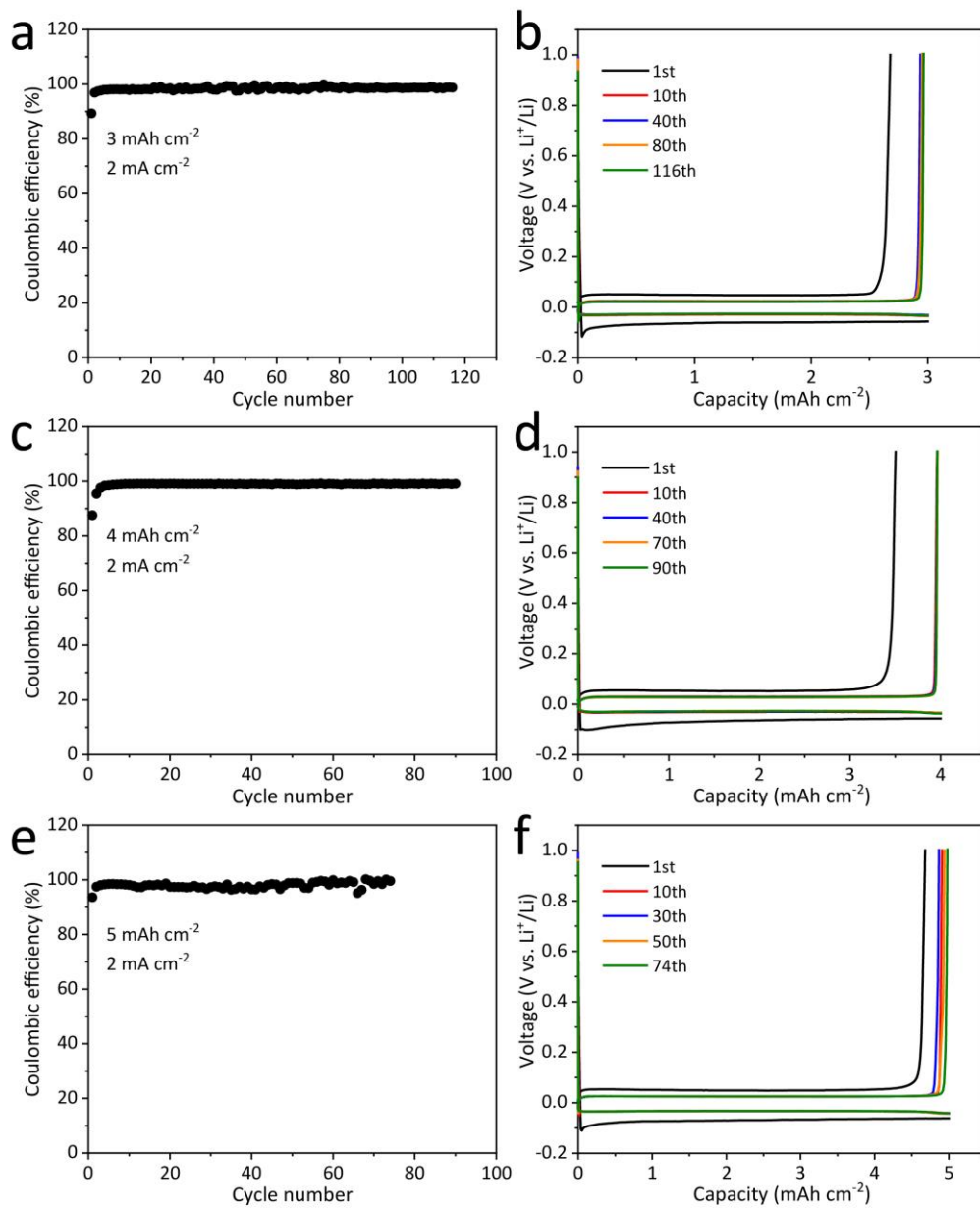
Figure S4. Coulombic efficiency evaluation and voltage profiles of the Li plating/stripping process on the Ni macropore array electrode measured at 2 mA cm^{-2} for (a, b) 3 mAh cm^{-2}, (c, d) 4 mAh cm^{-2} and (e, f) 5 mAh cm^{-2}. The amounts of electrolyte used in the assembly of half cells cycling at various capacities were 0.029, 0.022 and 0.018 mL mAh^{-1}

corresponding to the cycling capacities of 3, 4 and 5 mAh cm^{-2}, respectively. Related to
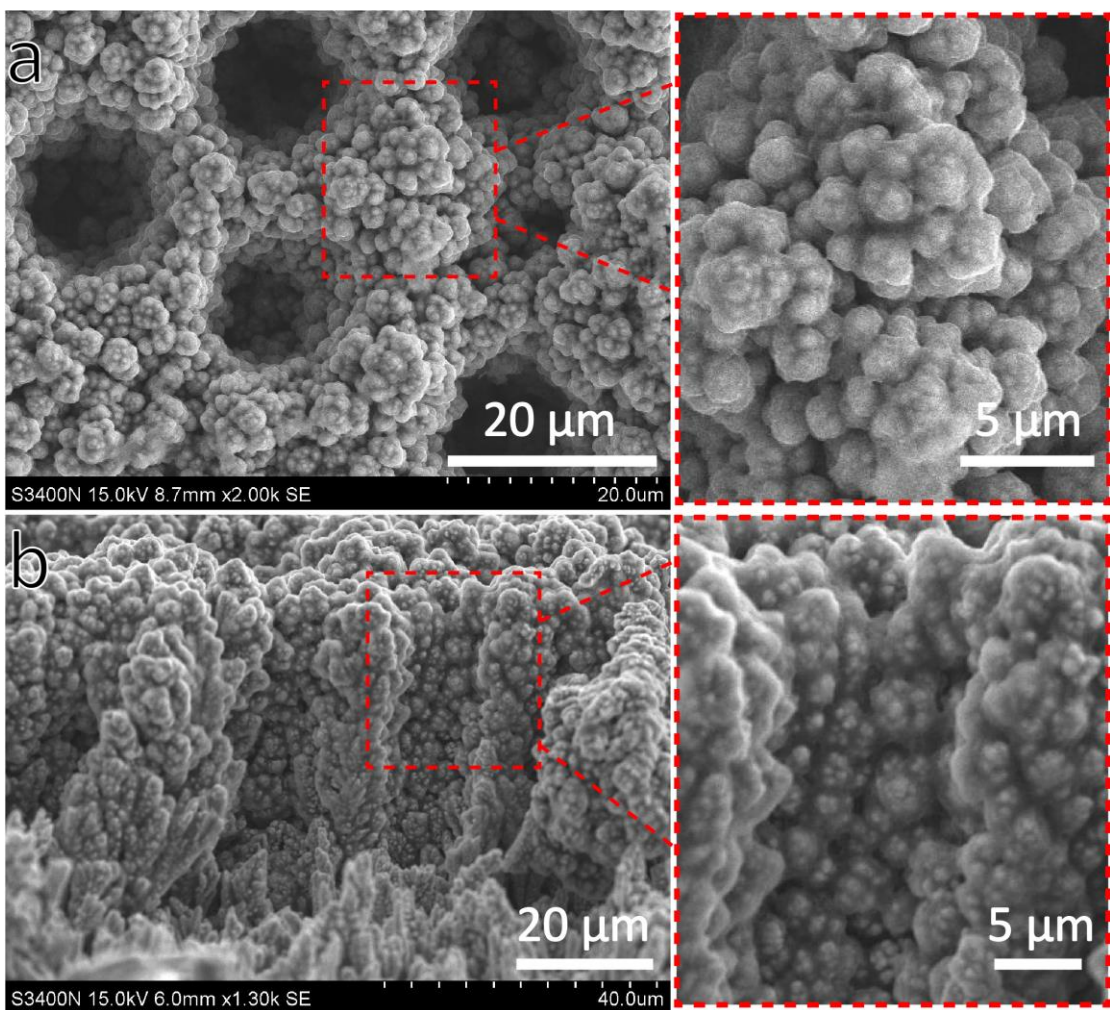
Figure 3.

Figure S5. (a) The surface SEM image and (b) the cross-sectional SEM image of the Ni macropore array electrode after 50 cycles. Related to Figure 4.
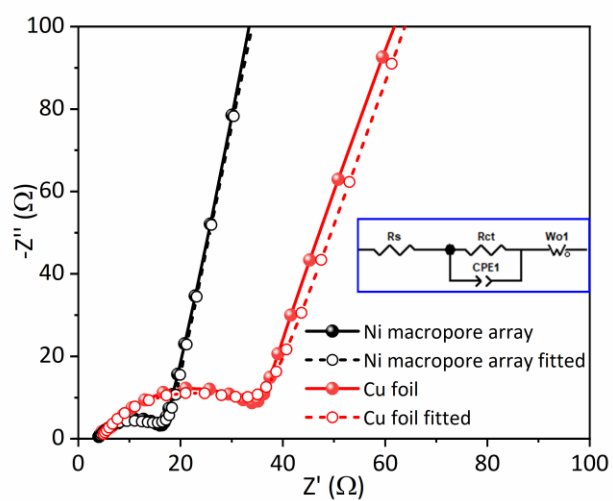
Figure S6. EIS and fitting results of the Ni macropore array and Cu foil electrodes after 100 cycles (inset is the equivalent circuit model). Related to Figure 4.

Table S2. Equivalent-circuit parameters obtained by fitting the experimental impedance spectra. Related to Figure 4.

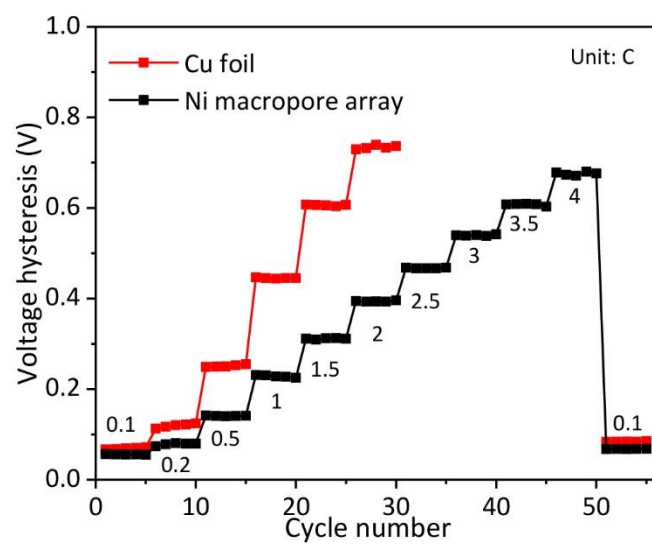| Sample	R_s (Ω)	Error	R_{ct} (Ω)	Error
Cu foil	4.06	3.43%	22.7	3.25%
Ni macropore array	3.80	1.49%	9.06	2.00%

Figure S7. Voltage hysteresis of full cells with Li-Ni macropore array anode and Li-Cu foil anode against LiFePO$_4$ cathode. Related to Figure 5.

Supplemental Reference

Li, Y., Jia, W.-Z., Song, Y.-Y., and Xia, X.-H. (2007). Superhydrophobicity of 3D Porous Copper Films Prepared Using the Hydrogen Bubble Dynamic Template. Chem. Mater. *19*, 5758-5764.

Sturm, J., Rheinfeld, A., Zilberman, I., Spingler, F.B., Kosch, S., Frie, F., and Jossen, A. (2019). Modeling and simulation of inhomogeneities in a 18650 nickel-rich, silicon-graphite lithium-ion cell during fast charging. J. Power Sources *412*, 204-223.

Zhang, Y.Q., Xia, X.H., Wang, X.L., Mai, Y.J., Shi, S.J., Tang, Y.Y., Gu, C.G., and Tu, J.P. (2012). Three-dimensional porous nano-Ni supported silicon composite film for high-performance lithium-ion batteries. J. Power Sources *213*, 106-111.